Effects of viscous heating and wall-fluid interaction energy on rate-dependent slip behavior of simple fluids

Luyao Bao,[1] Nikolai V. Priezjev,[2] Haibao Hu,[1,3,*] and Kai Luo[1]

[1]*School of Marine Science and Technology, Northwestern Polytechnical University, Xi'an, Shaanxi 710072, People's Republic of China*

[2]*Department of Mechanical and Materials Engineering, Wright State University, Dayton, Ohio 45435, USA*

[3]*Research & Development Institute in Shenzhen, Northwestern Polytechnical University, Shenzhen 518057, People's Republic of China*

(Received 29 May 2017; published 25 September 2017)

Molecular dynamics simulations are used to investigate the rate and temperature dependence of the slip length in thin liquid films confined by smooth, thermal substrates. In our setup, the heat generated in a force-driven flow is removed by the thermostat applied on several wall layers away from liquid-solid interfaces. We found that for both high and low wall-fluid interaction (WFI) energies, the temperature of the fluid phase rises significantly as the shear rate increases. Surprisingly, with increasing shear rate, the slip length approaches a constant value from above for high WFI energies and from below for low WFI energies. The two distinct trends of the rate-dependent slip length are rationalized by examining $S(\mathbf{G}_1)$, the height of the main peak of the in-plane structure factor of the first fluid layer (FFL) together with D_{WF}, which is the average distance between the wall and FFL. The results of numerical simulations demonstrate that reduced values of the structure factor, $S(\mathbf{G}_1)$, correlate with the enhanced slip, while smaller distances D_{WF} indicate that fluid atoms penetrate deeper into the surface potential leading to larger friction and smaller slip. Interestingly, at the lowest WFI energy, the combined effect of the increase of $S(\mathbf{G}_1)$ and decrease of D_{WF} with increasing shear rate results in a dramatic reduction of the slip length.

DOI: 10.1103/PhysRevE.96.033110

I. INTRODUCTION

Over the past decades, experiments [1–5] and molecular dynamics (MD) simulations [6–13] have demonstrated that the traditional no-slip boundary condition (BC) does not necessarily hold in small-scale systems that involve either hydrophobic surfaces or high shear rates. Application of the slip BC, instead of no-slip BC, in numerical models remediates the singular or unphysical behavior of fluid in some situations, such as droplet spreading [14–17] and corner flows [18,19]. Also, for micro- and nanoscale flows, interfacial slip can significantly affect the fluid transport due to the large surface-to-volume ratio in such systems [20–22]. Recent studies have demonstrated that water flows through a carbon nanotube nearly without friction because of the extremely "large" slip [23,24]. The concept of slip length, originally introduced by Navier, is commonly used to quantify the degree of slip. By definition, the slip length is the distance with respect to the wall-fluid interface where the linearly extrapolated fluid velocity profile reaches the velocity of wall. Typical values of slip length observed in experiments on fluids over smooth nonwetting surfaces are of the order of ten nanometers [1–4]. Complimentary to the experimental approach, MD simulations [6–13] were extensively used to study the slip behavior, since this method provides the detailed information about structure and dynamics of fluids near solid interfaces at the atomic level.

The MD studies of interfacial slip can be broadly categorized in two types depending on the procedure for removing the heat generated in the sheared fluid, as discussed in detail by Yong and Zhang [25]. The first type of procedure [6,7,12,25,26] is to extract the heat directly from the fluid phase by applying a thermostat to fluid atoms. This thermostatting strategy is referred to as TF (thermostat fluid). For TF, the wall model can be either rigid or flexible. When the flexible wall model is adopted, the thermostat is also applied to the wall atoms to ensure that the temperature of the system is properly controlled. The second type of procedure documented in the literature [9,27–31] involves the application of the thermostat only to the wall atoms; that is, the heat generated in the fluid is removed through the confining walls. This thermostat strategy is referred to as TW (thermostat wall), and, thus, only the flexible wall model can be used for TW.

The fluid temperature profiles strongly depend on the TF and TW protocols. In particular, for TF, the fluid temperature is spatially uniform and it remains nearly unchanged as shear rate increases. In contrast, for TW, the fluid temperature is usually distributed nonuniformly across the channel and it increases at higher shear rates due to viscous heating. The thermostatting strategy of TW closely resembles a laboratory condition, and, thus, it is expected to produce more tenable slip behavior [28,32]. However, it has been shown that the rate-dependent slip in systems with TF protocol is consistent with the results using TW at low shear rates [25], which can be attributed to negligible viscous heating at low shear rates.

When TF procedure is applied at low shear rates, it has been demonstrated that the slip length is inversely correlated to the degree of structure in the first fluid layer (FFL) induced by the periodic wall lattice [33–35]. The first fluid layer consists of fluid atoms confined between the solid wall and the first minimum in the fluid density profile perpendicular to the wall. The degree of the surface-induced structure in the FFL mainly depends on the wall-fluid interaction (WFI) energy and the commensurability of liquid and solid structures at the interface. In general, lower WFI energy results in less pronounced structure of the FFL [10,33–35], while highly incommensurable structures of the liquid and solid phases at the interface reduce the ordering within the FFL [33]. The surface topography also affects the velocity slip behavior.

*huhaibao@nwpu.edu.cn

Thus, Zhang and Chen [36,37] carried out a series of MD simulations on this topic using TF strategy. They found that, in comparison with the atomically smooth surface, a rough surface induces extra viscous dissipation in the flow leading to reduction in boundary slip. Moreover, a more irregular topography decreases boundary slip even for the same statistical roughness height [37]. Previous MD studies [38–40] have also demonstrated that the topography of surface has a significant influence on the temperature jump, which in turn affects the velocity slip [29].

At high shear rates, the functional form of the rate-dependent slip length depends on the details of the MD simulation model and the thermostatting procedure. The original MD study by Thompson and Troian [6] showed that, when TF is applied, the slip length increases as a power-law function of shear rate up to a critical value. The similar behavior of the slip length at high shear rates has been also observed in a number of MD studies using the TF strategy [7,10,12,41]. For example, when the WFI energy is relatively high, it was shown that the slip length increases linearly with shear rate [35], while generally the MD data for the rate-dependent slip length can be well fitted by a polynomial function [42]. On the other hand, other MD studies with thermal walls predicted that the slip length is saturated at high shear rates [9,27,43,44]. Using three methodologies, namely, MD simulations with TW, an analytical theory of slip, and a Navier-Stokes-based calculation, Martini *et al.* [28] determined that the slip length first increases and then approaches a constant value as the shear rate increases. Their results further indicate that the MD simulation model should accurately account for the heat transfer from the fluid phase to the solid walls at high shear rates. In other words, the TW strategy might be more appropriate to describe realistic slip behavior at high shear rates using MD simulations. Hence, the detailed analysis by Martini *et al.* [28] emphasized the inconsistency in the slip behavior at high shear rates.

Recently, Pahlavan and Freund [32] reported a counter-intuitive dependence of the slip length on shear rate using the TW strategy in MD simulations. More specifically, they found that the slip length decreases with increasing shear rate and asymptotes to the no-slip BC at high shear rates. One of the notable differences between the MD setups of Martini *et al.* [28] and Pahlavan and Freund [32], is the strength of the WFI. To address the contradictory results regarding the rate dependence of the slip length at high shear rates using the TW thermostat strategy, the effects of viscous heating, shear rate and WFI energy on the slip length have to be considered concomitantly.

In this paper, we examine the slip behavior in force-driven flows of simple fluids over smooth walls in the regime where viscous heating becomes important at high shear rates. It will be shown that the fluid temperature rises monotonically with increasing shear rate, which results in either decrease or increase of the slip length at low or high WFI energies. By examining $S(\mathbf{G}_1)$, the peak value of the in-plane structure factor of the FFL together with D_{WF}, the average distance between the wall and FFL, we will demonstrate that two distinct trends of the rate-dependent slip length originate from the combined influence of fluid temperature and shear rate on the parameters $S(\mathbf{G}_1)$ and D_{WF} at high and low WFI energies.

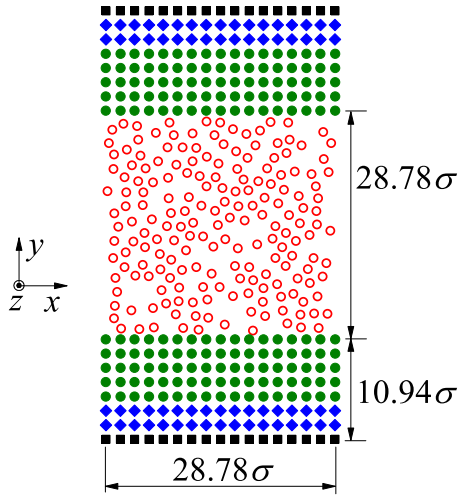

FIG. 1. The schematic diagram of the simulation domain. The symbol (○) denotes fluid atoms; the fluid phase consists of 19 652 atoms. Each wall consists of 25 000 atoms that form a faced-centered-cubic (001) structure with 20 layers and the lattice constant of $1.15\,\sigma$. There are three types of layers in both upper and lower walls; namely, fixed layers (■), thermostat layers (◆) and free layers (●). Note that only a reduced set of wall atoms in the thermostat and free layers are shown for clarity.

The paper is organized as follows. The details of MD simulations are given in the next section. The representative velocity and temperature profiles at different shear rates and WFI energies are examined in Sec. III A. The effects of shear rate and viscous heating on the slip length and Kapitza thermal resistance length are discussed in Secs. III B and III C. The analysis of the surface-induced fluid structure in the adjacent fluid layer is presented in Sec. III D. The summary is provided in Sec. IV.

II. DETAILS OF MD SIMULATIONS

The MD simulation model consists of the monatomic fluid confined between stationary thermal walls (see as Fig. 1). The pairwise interaction between atoms was modeled by the truncated Lennard-Jones (LJ) potential:

$$E_{ij} = 4\varepsilon_{\alpha\beta}\left[\left(\frac{\sigma_{\alpha\beta}}{r_{ij}}\right)^{12} - \left(\frac{\sigma_{\alpha\beta}}{r_{ij}}\right)^{6}\right], \tag{1}$$

where E_{ij} is energy between atoms i and j, and ε and σ are the characteristic energy and length of the LJ potential, respectively. Here, α and β are types of atoms i and j. The indices $\alpha\beta$ denote either fluid-fluid (FF), wall-fluid (WF), or wall-wall (WW), which correspond to the interaction between fluid atoms, between fluid and wall atoms, or between wall atoms. The LJ units defined by the intrinsic properties of the fluid phase: m_{FF}, $\varepsilon_{\mathrm{FF}}$, and σ_{FF} are used to express all physical units, and, in what follows, the subscripts will be omitted. The cutoff distance ($r_C = 2.5\sigma$) of the LJ potential was used to improve the computational efficiency.

The width of channel is fixed $H = 28.78\sigma$ along the y axis and the lateral dimensions are set $L_x = L_z = 28.78\sigma$. Periodic conditions are imposed along the x and z directions.

The density of fluid and wall are $\sim 0.83\sigma^{-3}$ and $\sim 2.76\sigma^{-3}$, respectively. To implement the so-called flexible wall model, the wall atoms were allowed to vibrate around their lattice sites. The characteristic energy and length of the LJ potential between wall atoms are $\varepsilon_{WW} = 50\varepsilon$ and $\sigma_{WW} = 0.7342\sigma$, respectively. The mass of wall atoms is $m_W = 4.94m$. These parameters were chosen to ensure that the ratio of the root-mean-square displacement ($\sqrt{\langle \Delta u^2 \rangle}$) of the wall atoms and their nearest-neighbor distance (d) was smaller than the Lindemann criterion for melting ($\sqrt{\langle \Delta u^2 \rangle}/d \lesssim 0.15$) [32,33,45] in all cases.

The top layer of the upper wall and the bottom layer of the lower wall were rigidly fixed during the entire simulation process to maintain the integrity of solid walls. These two layers are referred to as fixed layers (black squares in Fig. 1). The four layers adjacent to the fixed layer in each wall are referenced as thermostat layers (blue diamonds in Fig. 1). The other 15 wall layers in contact with the fluid phase are called free layers (green circles in Fig. 1).

The planar Poiseuille flow was induced by applying a constant external force F_x to each fluid atom in the +x direction. At the beginning of the simulation, the Nosé-Hoover thermostat was applied to the fluid atoms, thermostat layers, and free layers to equilibrate the system at the temperature of $0.75\,\varepsilon/k_B$, where k_B is the Boltzmann constant. After additional 5×10^5 MD time steps, the external force was applied to fluid atoms, and the thermostatting of fluid atoms and free layers was canceled. Thus, the viscous heat generated within the fluid was removed by the thermostat layers. The time interval of 10^6 MD time steps was used to reach the steady Poiseuille flow. The fluid velocity and temperature profiles were averaged within slices of thickness $\Delta y = 0.2\sigma$ for additional 2×10^6 MD time steps. The same time interval was used to average the fluid density profile with thinner slices $\Delta y = 0.02\sigma$. All MD simulations were carried out using the open-source LAMMPS MD code [46] with the time step $\Delta t = 0.002\tau$, where $\tau = \sqrt{(m\sigma^2/\varepsilon)}$ in the LJ time.

The slip length was computed using the relation $L_S = v_S/\dot{\gamma}$, where v_S and $\dot{\gamma}$ are the slip velocity and shear rate at the wall-fluid interface. The locations of the interfaces were defined at the lattice positions of the bottom layer of the upper wall and the top layer of the lower wall. The parameters v_S and $\dot{\gamma}$ were determined by extrapolating a parabolic fit of the velocity profile in the central part ($3.1\sigma \sim 25.7\sigma$) of the channel to the locations of the wall-fluid interfaces.

The Kapitza resistance length (L_K) was also computed to quantify the thermal resistance between the fluid phase and solid walls; a parameter which is analogous to the slip length [39,47,48]. The Kapitza resistance length was calculated using $L_K = T_J/\dot{T}$, where T_J and $\dot{T}$ are the temperature jump and the temperature gradient at the wall-fluid interface. Both parameters, T_J and $\dot{T}$, were determined by extrapolating a fourth-order polynomial fit of the temperature profile in the central part ($3.1\sigma \sim 25.7\sigma$) of the channel to the wall-fluid interfaces. Note, that $T_J = T_F|_{Wall} - T_W$, where $T_F|_{Wall}$ is the extrapolated temperature of the fluid phase at the wall-fluid interface and T_W is the temperature of the bottom layer of the upper wall and the top layer of the lower wall.

III. RESULTS AND DISCUSSION

A. Fluid velocity and temperature profiles

With increasing shear rate, the viscous heating effect in sheared fluids can be significant and the temperature profiles become spatially nonuniform [12,25,32,47,49,50]. For nanoconfined monatomic fluids, the velocity and temperature profiles in the central part of the channel are well described by the continuum fluid dynamics [35,51]. To remind, the solution of the Navier-Stokes and heat conduction equations for incompressible steady Poiseuille flow, with slip BC and the Kapitza thermal resistance, are given by

$$v_x(y) = \frac{\rho F_x H^2}{2\mu}\left[\frac{1}{4} - \left(\frac{y}{H} - \frac{1}{2}\right)^2\right] + v_S, \quad (2)$$

$$T(y) = \frac{\rho^2 F_x^2 H^4}{12\lambda\mu}\left[\frac{1}{16} - \left(\frac{y}{H} - \frac{1}{2}\right)^4\right] + T_J + T_W, \quad (3)$$

where H is the channel height and T_W is the wall temperature [52]. Here, μ and λ are the fluid shear viscosity and thermal conductivity, respectively.

Figure 2 shows representative velocity profiles in steady-state flow for four selected values of the external force F_x. The data for the WFI energy $\varepsilon_{WF} = 1.0\varepsilon$ and 0.3ε are presented only in a half of the channel because of the symmetry with respect to the mid-plane of the computational domain. As is evident, the fluid velocity profiles are well fitted by a parabola, as predicted by the continuum hydrodynamics [see Eq. (2)]. It can be clearly seen that the slip velocity v_S increases with the applied force for $\varepsilon_{WF} = 1.0\varepsilon$ and 0.3ε. The fluid slip velocity is larger for $\varepsilon_{WF} = 0.3\varepsilon$ and relatively small values of the external force $F_x \lesssim 0.2\,\varepsilon/\sigma$. By sharp contrast, larger slip is observed at interfaces with higher WFI energy ($\varepsilon_{WF} = 1.0\varepsilon$)

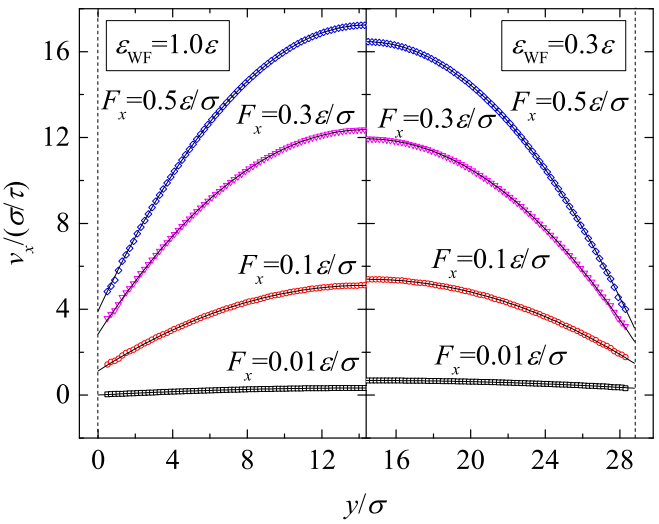

FIG. 2. The velocity profiles $v_x(y)$ for the indicated values of the applied force F_x for the wall-fluid interaction energies $\varepsilon_{WF} = 1.0\varepsilon$ (left) and 0.3ε (right). The solid curves represent a parabolic fit to the MD data in the central part of the channel ($3.1\sigma \sim 25.7\,\sigma$). The vertical dashed lines denote the location of wall-fluid interfaces at $y = 0\sigma$ and $y = 28.78\sigma$.

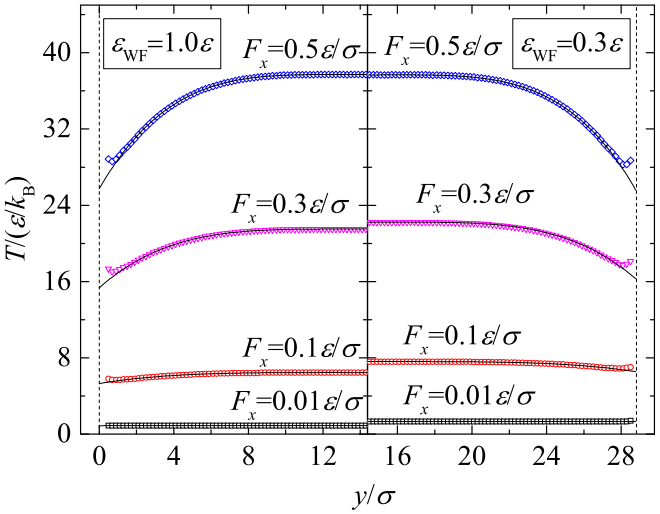

FIG. 3. The fluid temperature profiles $T(y)$ for the indicated values of the applied force F_x for the WFI energies $\varepsilon_{WF} = 1.0\varepsilon$ (left) and 0.3ε (right). The solid curves represent a fourth-degree polynomial fit to the MD data. The dashed lines indicate the location of wall-fluid interfaces at $y = 0\sigma$ and $y = 28.78\sigma$.

and larger external forces $F_x = 0.3\varepsilon/\sigma$ and $0.5\varepsilon/\sigma$. A more detailed analysis of the slip behavior for different flow conditions and WFI energies will be presented in the next section.

The viscous heating and the rate of the heat removal at different external forces and WFI energies determine fluid temperature profiles in steady state. For example, Fig. 3 shows the corresponding temperature profiles in steady flow for the same values of the external force F_x as in Fig. 2. Similarly, the data for WFI energies $\varepsilon_{WF} = 1.0\varepsilon$ and 0.3ε are also presented only in a half of the channel because of the symmetry. The temperature profiles, except near interfaces, are well described by a fourth-order polynomial, as expected from the continuum predictions [see Eq. (3)]. Note that the fluid temperature near the walls slightly increases and deviates from the theoretical prediction, which was also observed in the previous study [53].

Furthermore, it can be observed in Fig. 3 that the fluid temperature profiles are nearly flat at $F_x = 0.01\,\varepsilon/\sigma$ for $\varepsilon_{WF}= 1.0\varepsilon$ and 0.3ε, indicating that viscous heating is not significant at low shear rates. As F_x increases, the average temperature of the fluid increases and nonlinearity of the temperature profiles becomes more pronounced. In other words, viscous heating in the sheared fluid increases with the external force in both cases $\varepsilon_{WF} = 1.0\varepsilon$ and 0.3ε. At $F_x \lesssim 0.3\,\varepsilon/\sigma$, a reduced WFI leads to a more significant viscous heating since the Kapitza thermal resistance is expected to be larger at lower WFI energies [39,47,48]. However, at $F_x = 0.5\,\varepsilon/\sigma$, the temperature profiles are nearly the same for $\varepsilon_{WF} = 1.0\varepsilon$ and 0.3ε (see Fig. 3). These results suggest that the WFI strength and the external force, and the corresponding shear rate, have a nontrivial combined effect on the Kapitza thermal resistance, which will be discussed in more detail below.

We note that the average temperature of the fluid increases from $\sim 0.90\,\varepsilon/k_B$ to $\sim 36\,\varepsilon/k_B$ as F_x increases from $0.01\,\varepsilon/\sigma$ to $0.5\,\varepsilon/\sigma$ at different WFI energies. A similar increase in the fluid temperature at high shear rates was also observed in the previous MD studies using the TW thermostatting strategy [12,29,49,50]. In contrast, the average temperature of the solid walls increases from $\sim 0.75\,\varepsilon/k_B$ to $\sim 2.0\,\varepsilon/k_B$, while it should be emphasized that they remain rigid for all flow conditions considered in the present study. The significant variation of the fluid temperature affects the state of the fluid on the phase diagram. Below, we include a comment on this issue.

By modifying the 33-parameter Benedict-Webb-Rubin (MBWR) equation, Nicolas *et al.* [54] have developed an equation of state for the LJ fluid. Later, Johnson *et al.* [55] improved the equation of Nicolas *et al.* [49] using more accurate MD simulation results. Using the MBWR equation of Johnson *et al.* [55] and the Maxwell construction, Cosden [56] numerically calculated the liquid-vapor coexistence (binodal) curve, which was plotted along with the spinodal curve in the density-temperature phase diagram [57]. In our study, the bulk density and the average temperature of the fluid are $\sim 0.83\,\sigma^{-3}$ and $\sim 0.90\,\varepsilon/k_B$ at the lowest shear rate for different WFI energies. According to the phase diagram of Cosden, the phase state of fluid at these conditions is clearly above the coexistence curve and below the critical point, indicating that the fluid is a stable liquid [58]. As the shear rate increases, the average temperature of fluid increases significantly, while the variation of the fluid bulk density is less than $0.05\,\sigma^{-3}$. Thus, when the average fluid temperature T_{ave} increases but remains below the temperature of the critical point T_C ($\sim 1.3\,\varepsilon/k_B$), the state of fluid remains a stable liquid [58]. As T_{ave} increases above T_C with increasing shear rate, the state of fluid enters into the supercritical fluid-phase region on the phase diagram [58].

The dramatic increase of the average fluid temperature with increasing shear rate influences the fluid viscosity, which might also depend on the position relative to the walls. In a force-driven flow, the viscosity of the fluid at different locations along the y-axis can be computed using the following equation:

$$\mu(y_1) = \mu(y_2) = \frac{F_x \Delta y A \sum_{i=1}^{n} \rho_i}{(\dot{\gamma}_1 + \dot{\gamma}_2)A}, \tag{4}$$

where Δy is the thickness of a slice parallel to the lattice plane, A is the area of simulation domain in the xz plane. Here, $\dot{\gamma}_1$ and $\dot{\gamma}_2$ are shear rates of the fluid phase at y_1 and y_2, respectively. The locations y_1 and y_2 are symmetrical with respect to the midplane of the fluid phase whose y coordinate can be set at the center of the channel, i.e., at $14.39\,\sigma$. In our calculations, y_1 increases from 3.1σ to $11.9\,\sigma$ in slices of thickness $0.2\,\sigma$, and correspondingly, y_2 decreases from $25.7\,\sigma$ to $16.9\,\sigma$. For given external force and WFI energy, it can be seen from Fig. 3 that the temperature profile of the fluid is nearly flat in the center of channel, which means the shear viscosity is position independent in the center of channel. Therefore, the shear viscosity was evaluated in the region where the nonlinearity of the temperature profiles is pronounced. In our flow geometry, the shear viscosity μ was evaluated in 45 adjacent slices parallel to walls.

Figure 4 shows the average values of μ for different external forces and WFI energies. To make a comparison with the results of the previous study [49], the data in Fig. 4 are plotted as a function of the interfacial shear rate $\dot{\gamma}$ for each ε_{WF}. The error bars represent the standard deviation of 45 values of μ at each ε_{WF}. It can be clearly seen that the values of the standard deviation are small in comparison with the average values of

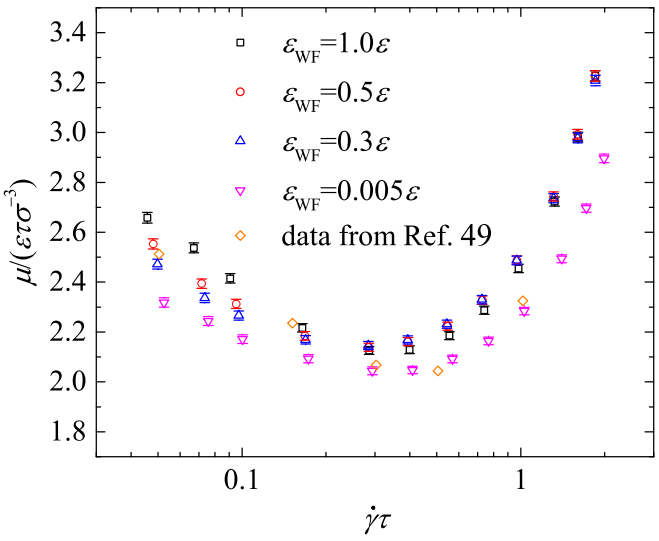

FIG. 4. The fluid viscosity μ as a function of the interfacial shear rate $\dot{\gamma}$ for the indicated values of the wall-fluid interaction energy ε_{WF}. The error bars represent the standard deviation of 45 values.

μ. Therefore, the viscosity of the fluid does not depend on the location of the averaging bin inside the channel for given values of $\dot{\gamma}$ (or external force) and ε_{WF}. In other words, the fluid shear viscosity is spatially uniform for given values of $\dot{\gamma}$ (or external force) and ε_{WF}. At a given ε_{WF}, the fluid viscosity is negatively (positively) correlated with the interfacial shear rate $\dot{\gamma}$, when $\dot{\gamma}$ is smaller (larger) than $\sim 0.3\tau^{-1}$, respectively. A similar relationship between the fluid viscosity and interfacial shear rate was also reported in the previous study [49].

The influence of $\dot{\gamma}$ on the fluid viscosity can be understood by considering the fluid temperature and the corresponding fluid state on the phase diagram. As discussed above, at low interfacial shear rates, the fluid is in a liquid state whose viscosity is dominated by attractive LJ forces [59,60]. Thus, with increasing shear rate, higher temperature results in smaller sizes of coherent groups of atoms because of the increased agitation of individual atoms, and, consequently, there is less resistance to deformation in the liquid, i.e., smaller viscosity [59]. At higher shear rates, the temperature of the fluid increases significantly and the momentum transport is mainly governed by the repulsive part of the LJ potential [60]. Thus, the shear viscosity of the LJ fluid at high temperatures is similar to that of the soft-sphere system, i.e., $\mu \sim \rho T^{5/12}$ [60]. Therefore, the increase in the fluid temperature leads to larger fluid viscosity at high shear rates. Taken together, the shear viscosity first decreases and then increases with increasing shear rate and, as a result, fluid temperature, i.e., the minima appear in the dependence of viscosity as a function of shear rate, as shown in Fig. 4.

As shown in Fig. 4, at $\dot{\gamma} \lesssim 0.3\tau^{-1}$, i.e., relatively low shear rates, the fluid viscosity is smaller for lower ε_{WF} at a given $\dot{\gamma}$ because lower WFI results in higher temperature of the fluid (see Fig. 3). At $\dot{\gamma} \gtrsim 0.3\tau^{-1}$, the shear viscosity is nearly the same for $\varepsilon_{WF} \gtrsim 0.3\varepsilon$ for a given $\dot{\gamma}$ because of the negligible difference in the fluid temperature in these cases [Figs. 3 and 6(a) presented in Sec. III C]. For $\varepsilon_{WF} = 0.005\varepsilon$, the fluid viscosity is smaller than for $\varepsilon_{WF} = 1.0\varepsilon \sim 0.3\varepsilon$ at both low and high shear rates due to the lower fluid temperature [see Fig. 6(a) presented in Sec. III C]. Another contributing factor leading to smaller values of the shear viscosity in the case $\varepsilon_{WF} = 0.005\varepsilon$ is that the FFL is displaced closer to the walls, which effectively increases the channel height and, consequently, reduces viscosity [13].

B. The rate-dependence of the slip length for high and low WFI energies

Figure 5(a) shows the slip length L_S as a function of the interfacial shear rate $\dot{\gamma}$ for different WFI energies ε_{WF}. It is clearly seen that in all cases the slip length depends strongly on shear rate. However, the relationships between the slip length and shear rate show opposite trends for high and low WFI energies. Thus, for high WFI energies $\varepsilon_{WF} = 1.0\varepsilon$ and 0.9ε, the slip length saturates asymptotically to a constant value. At $\dot{\gamma} \lesssim 1.0\tau^{-1}$, the slip length is larger for $\varepsilon_{WF} = 0.9\varepsilon$ than for $\varepsilon_{WF} = 1.0\varepsilon$ for a given value of the interfacial shear rate, while at higher shear rates, $\dot{\gamma} \gtrsim 1.0\tau^{-1}$, the slip length is nearly the same for $\varepsilon_{WF} = 0.9\varepsilon$ and 1.0ε. A similar positive correlation between the slip length and shear rate was also observed in thin films of n-decane confined by solid walls with the WFI energy of about 3.0ε when the TW thermostat was used in the Couette cell [28].

As shown in Fig. 5(a), an opposite correlation emerges at low WFI energies $\varepsilon_{WF} = 0.5\varepsilon$ and 0.3ε; namely, the slip length decreases monotonically with increasing interfacial shear rate. Moreover, the slip length decreases faster at $\varepsilon_{WF} = 0.3\varepsilon$ than at $\varepsilon_{WF} = 0.5\varepsilon$. Note that at $\dot{\gamma} \lesssim 0.55\tau^{-1}$, the slip length is larger at the lower WFI energy [see Fig. 5(a)]. This behavior is intuitively expected since interfaces with lower WFI energies result in larger slip lengths, if the WFI is sufficiently strong [13]. However, as shown in Fig. 5(a), the slip length can be smaller at lower WFI energies at very high shear rates. For example, for $\varepsilon_{WF} = 0.5\varepsilon$, the slip length is smaller than L_S for $\varepsilon_{WF} = 0.9\varepsilon$ and 1.0ε at $\dot{\gamma} \gtrsim 1.2\tau^{-1}$. This behavior is consistent with the results reported for the fluid velocity profiles in Fig. 2 for high and low WFI energies. Note also that the slip length is smaller for $\varepsilon_{WF} = 0.3\varepsilon$ than for $\varepsilon_{WF} = 0.5\varepsilon$ at $\dot{\gamma} \gtrsim 0.5\tau^{-1}$ [see Fig. 5(a)].

In the case of the lowest WFI energy, $\varepsilon_{WF} = 0.005\varepsilon$, the decay rate of the slip length is the largest and L_S asymptotes to a small but non-zero value ($\sim 0.34\sigma$). It is interesting to note that the slip length is smaller for $\varepsilon_{WF} = 0.005\varepsilon$ than for $\varepsilon_{WF} = 0.3\varepsilon$ in the range of accessible shear rates, which is different from the cases $\varepsilon_{WF} = 0.3\varepsilon$ and $\varepsilon_{WF} = 0.5\varepsilon$. This behavior is consistent with the results of the previous MD study where similar parameters of the fluid and solid phases were used but with the rigid wall model and TF thermostat [13]. In particular, it was demonstrated in Ref. [13] that the slip length acquires a distinct maximum at the critical value of the WFI energy ($\varepsilon_{CR} \sim 0.06\varepsilon$) that separates the positive and negative correlations between the slip length and WFI energy. In other words, the slip length first increases and then decreases when the WFI energy is reduced [13]. Thus, the results presented in Fig. 5(a) indicate that the nonmonotonic dependence of the slip length as a function of the WFI energy still holds at high shear rates for the system with the flexible wall model and the TW thermostatting strategy.

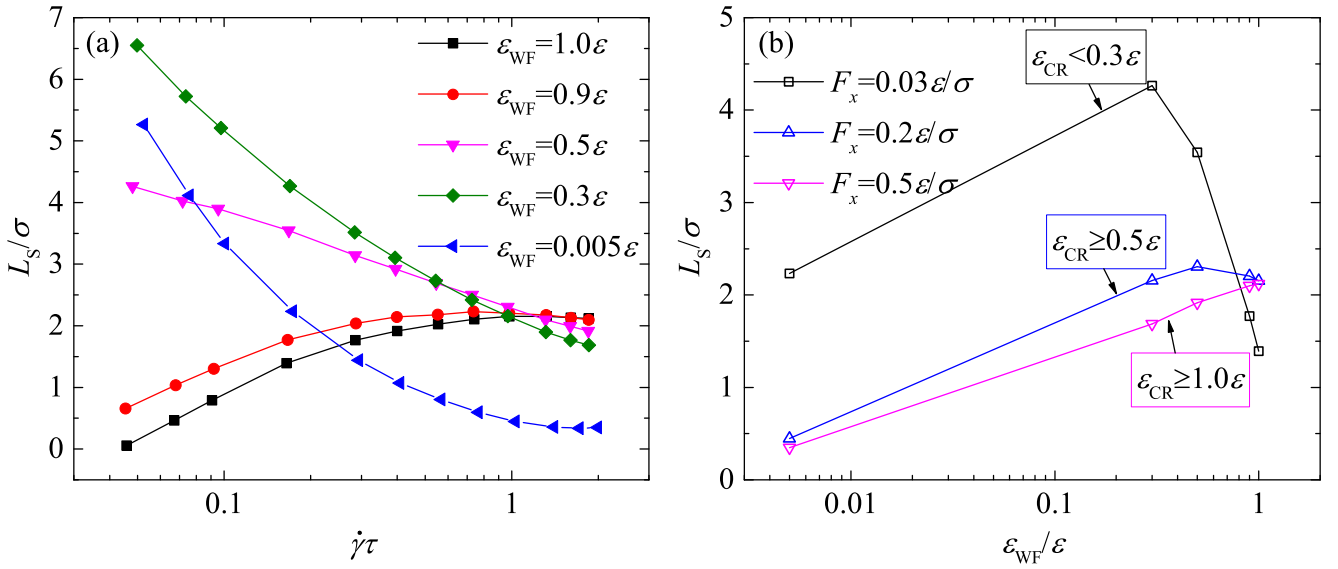

FIG. 5. (a) Variation of the slip length (L_S) as a function of the interfacial shear rate ($\dot{\gamma}$) for different values of the wall-fluid interaction energy (ε_{WF}). (b) The same as (a) but the selected data for L_S are replotted as a function of ε_{WF} for the indicated values of F_x.

Figure 5(b) shows the same data for the slip length but replotted as a function of the WFI energy for the indicated values of F_x. In the present study, the value of ε_{CR} was not determined accurately since only 5 different values of the WFI energy were considered. However, the qualitative trends of ε_{CR} dependence on the external force and fluid temperature can be easily deduced from the limited data. Following the conclusions from Ref. [13], it can be seen in Fig. 5(b) that the magnitude of ε_{CR} is smaller than 0.3ε for the case of $F_x = 0.03\varepsilon/\sigma$. As F_x increases to $0.2\varepsilon/\sigma$, the slip length is maximum when $\varepsilon_{WF} \sim 0.5\varepsilon$, and, hence, the value of ε_{CR} should be greater than 0.5ε [see Fig. 5(b)]. In the case of the largest external force $F_x = 0.5\varepsilon/\sigma$, the slip length decreases monotonically as WFI decreases from 1.0ε to 0.005ε, indicating that ε_{CR} is greater than 1.0ε. Therefore, we conclude that the critical value ε_{CR} increases with increasing external force, which in turn leads to higher fluid temperature in the MD setup with the TW strategy used in the present study. The relationship between ε_{CR} and the fluid temperature is consistent with the previous findings [13] that the positive correlation between ε_{CR} and the fluid temperature originates from the fact that the FFL is displaced closer to the wall at higher T.

C. Viscous heating at different interfacial shear rates and WFI energies

We next perform a detailed analysis of the viscous heating effect when the shear rate increases at different WFI energies

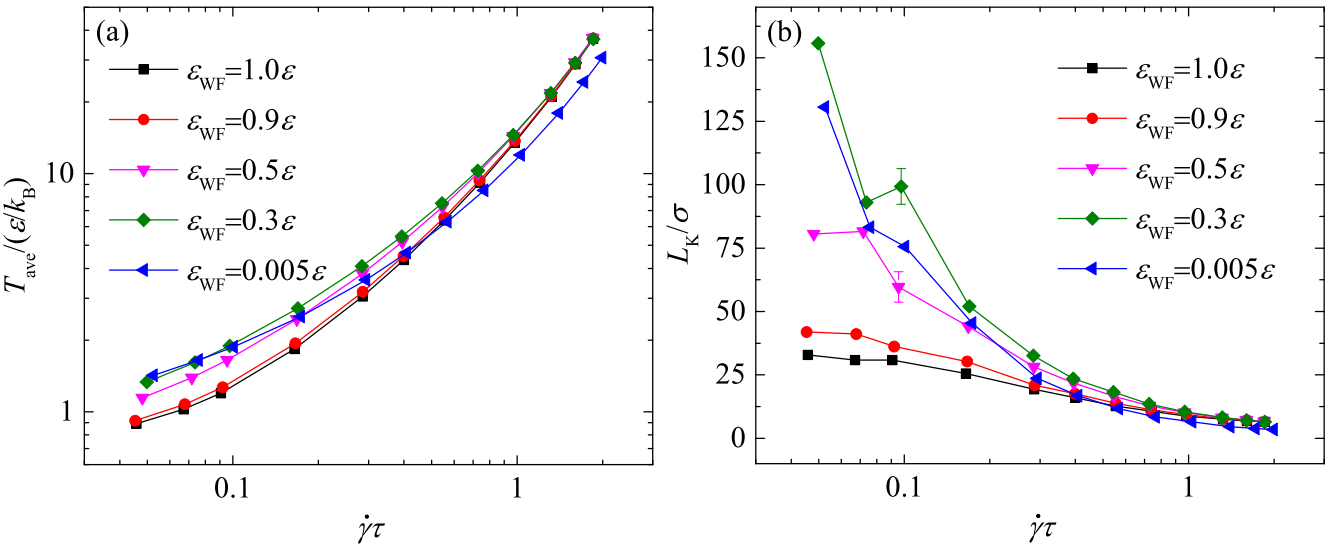

FIG. 6. (a) The temperature jump (T_J) and (b) the Kapitza thermal resistance (L_K) versus the interfacial shear rate ($\dot{\gamma}$) for the indicated values of the wall-fluid interaction energy (ε_{WF}).

by examining the average fluid temperature (T_{ave}) and the Kapitza thermal resistance length (L_K). It can be seen in Fig. 6(a) that T_{ave} increases dramatically at higher shear rates indicating that significant viscous heating occurs in the sheared fluid. At different WFI energies, L_K decreases monotonically as the interfacial shear rate increases [see Fig. 6(b)], which indicates that the efficiency of thermal transport between the fluid and wall becomes higher with increasing viscous heating, i.e., the average temperature of the fluid.

At relatively low interfacial shear rates, such as $\dot{\gamma} \approx 0.04\tau^{-1}$, T_{ave} increases as the WFI energy decreases from 1.0ε to 0.3ε [see Fig. 6(b)]. This behavior is consistent with the observation that L_K is larger at lower WFI energies, which demonstrates that the lower WFI energy results in less efficient thermal transport between the fluid and wall. Furthermore, as the interfacial shear rate increases, the differences in T_{ave} and L_K at different WFI energies ($\varepsilon_{WF} = 1.0\varepsilon \sim 0.3\varepsilon$) become reduced. In particular, at higher shear rates, $\dot{\gamma} \approx 1.6\tau^{-1}$ or $1.8\tau^{-1}$, such differences in T_{ave} and L_K are negligible for $\varepsilon_{WF} = 1.0\varepsilon \sim 0.3\varepsilon$. This behavior is consistent with the results reported Fig. 3 that the fluid temperature profiles are the approximately same at large external forces.

In the case of the lowest WFI energy $\varepsilon_{WF} = 0.005\varepsilon$, the average fluid temperature increases slower with increasing shear rate than in the other cases of WFI energy [see Fig. 6(a)]. Correspondingly, the Kapitza thermal resistance length decreases faster with increasing shear rate for $\varepsilon_{WF} = 0.005\varepsilon$. In contrast to the cases $\varepsilon_{WF} = 1.0\varepsilon \sim 0.3\varepsilon$, both T_{ave} and L_K are smaller at high shear rates $\dot{\gamma} \approx 1.6\tau^{-1}$ or $1.8\tau^{-1}$ for $\varepsilon_{WF} = 0.005\varepsilon$. We finally comment that the reported rate dependence of T_{ave} and L_K is related to the relatively low values of the fluid viscosity for $\varepsilon_{WF} = 0.005\varepsilon$ (shown in Fig. 4).

D. The analysis of the fluid structure near solid walls

In this section, the two opposite trends of the rate-dependent slip length are analyzed by examining the influence of the viscous heating effect on the properties of the FFL at different interfacial shear rates and WFI energies.

In general, the velocity slip in fluid flows over flexible walls can be strongly influenced by the lattice structure and the relative position of the FFL with respect to the adjacent wall layer. The lattice structure and WFI strength determine the potential energy landscape that induces a higher-order structure in the FFL, which in turn is found to be inversely correlated with the slip length [10,12,32–34,45]. The location of the FFL is also correlated with the slip length as it reflects the strength of the coupling between fluid and solid phases [32,45]. In the present study, the lattice structure of confining walls remains unchanged for all flow conditions. However, for a given WFI energy, the fluid temperature in contact with solid walls increases significantly at high shear rates, which affects the induced order within the FFL. In addition, the increase in fluid temperature, and, therefore, fluid pressure, leads to the displacement of the FFL closer to the adjacent wall layer. This effect becomes especially pronounced at low WFI energies [13,32]. As a result, the fluid atoms in the FFL penetrate slightly deeper into the wall structure leading to larger friction and, consequently, reduced slip [61].

The induced structure in the FFL can be quantitatively measured using the concept of the in-plane static structure factor, $S(\mathbf{k})$. It has been demonstrated in the previous MD studies [10,12,32–34,45] that the slip length is inversely correlated with the magnitude of the main peak of the in-plane static structure factor of the FFL, $S(\mathbf{G}_1)$, where $\mathbf{G}_1$ is the shortest reciprocal-lattice vector. The in-plane static structure factor is given by [33,45]

$$S(\mathbf{k}) = \frac{1}{N}\left|\sum_j e^{i\mathbf{k}\cdot\mathbf{r}_j}\right|^2,$$

where $\mathbf{r}_j = (x_j, z_j)$ is the two-dimensional position vector of the jth atom and the sum is taken over N atoms within the FFL. Here, $\mathbf{k} = (k_x, k_z)$ is the reciprocal vector parallel to the walls. In a finite system, the components of the vector $\mathbf{k}$ are restricted to integer multiples of $2\pi/L$, where L is the system size in the x and z directions [52]. Thus, the larger the system size, the smaller the values of k_x and k_z can be.

The quantity $S(\mathbf{G}_1)$ depends on the system size and the number of atoms. In our simulations, the average number of fluid atoms in the FFL depends of the fluid temperature and WFI energy. Therefore, the size-independent quantity $S(\mathbf{G}_1)/S(0)$, averaged over 100τ, was used in our analysis to correlate the fluid structure with the slip length. In addition, we measured how close, on average, the fluid atoms are located near the solid wall by computing the distance between the time-averaged center-of-mass (COM) of the FFL and the innermost wall layer, D_{WF}.

Figures 7(a) and 7(b) shows the variation of $S(\mathbf{G}_1)/S(0)$ and D_{WF} as a function of the interfacial shear rate for different WFI energies. We first discuss the correlation between $S(\mathbf{G}_1)/S(0)$, D_{WF} and the slip length at high WFI energies. For $\varepsilon_{WF} = 1.0\varepsilon$ and 0.9ε, the surface-induced structure in the FFL, $S(\mathbf{G}_1)/S(0)$, decreases significantly as the interfacial shear rate increases from $0.045\tau^{-1}$ to $1.8\tau^{-1}$ [see Fig. 7(a)]. At the same time, D_{WF} remains nearly shear-rate-independent for $\dot{\gamma} \lesssim 0.5\tau^{-1}$. These results imply that the increase in fluid temperature is not sufficiently large to displace the FFL towards the walls because of the relatively steep surface potential at high WFI energies. Therefore, it can be concluded that, as the shear rate increases up to $\dot{\gamma} \lesssim 0.5\tau^{-1}$, the decrease in $S(\mathbf{G}_1)/S(0)$ correlates inversely with increasing slip length, which is consistent with the previous MD results [33–35]. At $\dot{\gamma} \gtrsim 0.5\tau^{-1}$, D_{WF} decreases slightly with increasing shear rate because of the very high fluid temperature, which counterbalances the influence of the reduced structure $S(\mathbf{G}_1)/S(0)$ on the slip length. As a consequence, the rate of the slip length increase becomes slower at $\dot{\gamma} \gtrsim 0.5\tau^{-1}$, and L_S asymptotes to a constant value at high shear rates [see Fig. 5(a)].

At the lower WFI energy $\varepsilon_{WF} = 0.5\varepsilon$, $S(\mathbf{G}_1)/S(0)$ decreases more slowly with increasing shear rate than in the cases $\varepsilon_{WF} = 1.0\varepsilon$ and 0.9ε. As shown in Fig. 7(a), at $\varepsilon_{WF} = 0.3\varepsilon$, $S(\mathbf{G}_1)/S(0)$ is nearly shear-rate-independent. Therefore, the variation of $S(\mathbf{G}_1)/S(0)$ with increasing shear rate cannot explain the negative correlation between the slip length and the external force or the interfacial shear rate [see Fig. 5(a)]. Instead, the increase in pressure due to high fluid temperature causes the displacement of the FFL towards the wall because

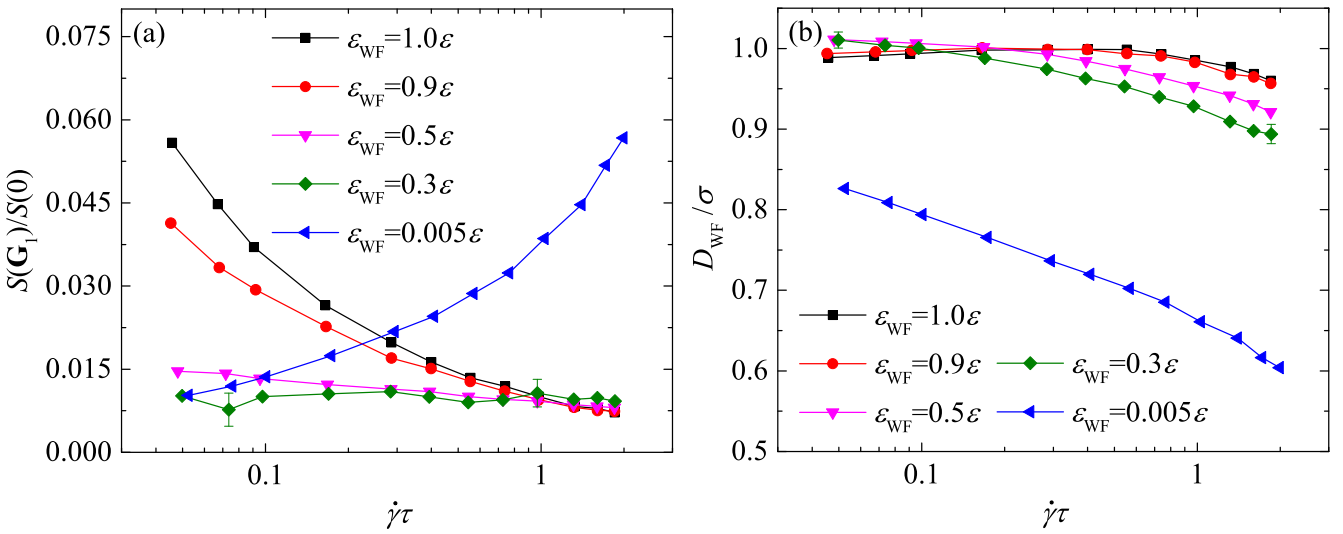

FIG. 7. (a) The normalized peak value of the in-plane static structure factor computed in the first fluid layer, $S(\mathbf{G}_1)/S(0)$, versus the interfacial shear rate ($\dot{\gamma}$) for the indicated values of the wall-fluid interaction energy (ε_{WF}). (b) Variation of D_{WF} as a function of $\dot{\gamma}$ for the same ε_{WF}.

of the relatively soft surface potential at low WFI energies. As shown in Fig. 7(b), D_{WF} decreases with increasing interfacial shear rate for $\varepsilon_{WF} = 0.5\varepsilon$ and 0.3ε. Note also that this trend becomes more evident in the case of the lower WFI energy, $\varepsilon_{WF} = 0.3\varepsilon$, where D_{WF} decreases faster with increasing shear rate than for $\varepsilon_{WF} = 0.5\varepsilon$, because of the softer surface potential. As discussed above, smaller values of D_{WF} reflect the fact that fluid atoms, on average, penetrate deeper into the adjacent wall layer causing larger friction between the fluid and wall. Thus, the decrease in D_{WF} results in the negative correlation between the slip length and the interfacial shear rate at low WFI energies as shown in Fig. 5(a).

In the case of the lowest WFI energy, $\varepsilon_{WF} = 0.005\varepsilon$, it can be observed in Fig. 7(a) that the structure factor $S(\mathbf{G}_1)/S(0)$ is relatively small, and it is nearly the same as in the case $\varepsilon_{WF} = 0.3\varepsilon$ at the low shear rate $\dot{\gamma} \approx 0.045\tau^{-1}$. However, $S(\mathbf{G}_1)/S(0)$ increases quickly with increasing shear rate at $\varepsilon_{WF} = 0.005\varepsilon$, which is markedly different from the case $\varepsilon_{WF} = 0.3\varepsilon$. It was previously shown that the FFL is displaced closer to the wall with increasing fluid temperature at the lowest value of the WFI energy $\varepsilon_{WF} = 0.005\varepsilon$ [13]. This behavior is consistent with the distinct negative correlation between D_{WF} and $\dot{\gamma}$ at $\varepsilon_{WF} = 0.005\varepsilon$ [shown in Fig. 7(b)]. Altogether, the positive correlation $S(\mathbf{G}_1)/S(0) \sim \dot{\gamma}$ and the negative correlation $D_{WF} \sim \dot{\gamma}$ both contribute to the decay of the slip length with increasing $\dot{\gamma}$ for $\varepsilon_{WF} = 0.005\varepsilon$ [see Fig. 5(a)].

IV. CONCLUSIONS

In summary, the effect of viscous heating on liquid slip over smooth surfaces with high and low WFI energies was studied using molecular dynamics simulations. The monatomic fluid was adopted to model a planar Poiseuille flow induced by a constant force. In steady-state flow, the heat in the fluid phase was removed by the thermostat applied to several layers within the solid walls, thus leaving unaffected the dynamics of wall and fluid atoms at interfaces. The values of interfacial shear rate and slip length were computed from the parabolic fits of the velocity profiles.

It was shown that the average fluid temperature rises significantly as the shear rate increases for both high and low WFI energies. Moreover, with increasing shear rate, the slip length asymptotes to a constant value from below (above) for high (low) WFI energies. These trends were analyzed by examining the influence of fluid temperature and shear rate on $S(\mathbf{G}_1)/S(0)$, the normalized main peak of the in-plane structure factor of the FFL, and D_{WF}, the distance between the wall and FFL. We found that slip is enhanced when $S(\mathbf{G}_1)/S(0)$ is reduced, while smaller values of D_{WF} imply that fluid atoms penetrate deeper into adjacent wall layer resulting in larger interfacial friction and, consequently, smaller slip lengths.

More specifically, at high WFI energies and low shear rates, $S(\mathbf{G}_1)/S(0)$ decreases quickly with increasing shear rate, but D_{WF} remains unchanged despite increasing fluid temperature, which altogether leads to the positive correlation between slip length and shear rate. At very high shear rates, the fluid temperature is extremely high so that D_{WF} decreases slightly with increasing shear rate, which counterbalances the influence of the reduced parameter $S(\mathbf{G}_1)/S(0)$ on slip length. As a consequence, the slip length increases slowly at very high shear rates and high WFI energies. In contrast, at low WFI energies, the increase in shear rate, which is accompanied by rising fluid temperature, does not affect $S(\mathbf{G}_1)/S(0)$ significantly. On the other hand, D_{WF} decreases monotonically with increasing shear rate. Therefore, the slip length correlates negatively with increasing shear rate at low WFI energies. Notably, in the case of the lowest WFI energy, the increase of $S(\mathbf{G}_1)/S(0)$ and, at the same time, decrease of D_{WF} with shear rate result in the sharp decrease of the slip length. These findings open perspectives for modeling complex systems with combined effects of rate dependence, viscous heating and wettability.

ACKNOWLEDGMENTS

This work was supported by the National Natural Science Foundation of China (Grant No. 51679203) and Natural Science Basic Research Plan in Shenzhen City of China(Grant No. JCYJ20160510140747996).

[1] R. Pit, H. Hervet, and L. Leger, Phys. Rev. Lett. **85**, 980 (2000).
[2] V. S. J. Craig, C. Neto, and D. R. M. Williams, Phys. Rev. Lett. **87**, 054504 (2001).
[3] E. Bonaccurso, M. Kappl, and H. J. Butt, Phys. Rev. Lett. **88**, 076103 (2002).
[4] C. H. Choi, K. J. A. Westin, and K. S. Breuer, Phys. Fluids **15**, 2897 (2003).
[5] C. Neto, D. R. Evans, E. Bonaccurso, H. J. Butt, and V. S. J. Craig, Rep. Prog. Phys. **68**, 2859 (2005).
[6] P. A. Thompson and S. M. Troian, Nature **389**, 360 (1997).
[7] N. V. Priezjev and S. M. Troian, Phys. Rev. Lett. **92**, 018302 (2004).
[8] D. M. Huang, C. Sendner, D. Horinek, R. R. Netz, and L. Bocquet, Phys. Rev. Lett. **101**, 226101 (2008).
[9] A. Martini, A. Roxin, R. Q. Snurr, Q. Wang, and S. Lichter, J. Fluid Mech. **600**, 257 (2008).
[10] X. Yong and L. T. Zhang, Phys. Rev. E **82**, 056313 (2010).
[11] F. C. Wang and Y. P. Zhao, Soft Matter **7**, 8628 (2011).
[12] X. Yong and L. T. Zhang, Microfluid. Nanofluid. **14**, 299 (2013).
[13] H. Hu, L. Bao, N. V. Priezjev, and K. Luo, J. Chem. Phys. **146**, 034701 (2017).
[14] P. A. Thompson and M. O. Robbins, Phys. Rev. Lett. **63**, 766 (1989).
[15] P. A. Thompson, W. B. Brinckerhoff, and M. O. Robbins, J. Adhes. Sci. Technol. **7**, 535 (1993).
[16] A. J Koplik and J. R. Banavar, Annu. Rev. Fluid Mech. **27**, 257 (2003).
[17] L. Bocquet and J.-L. Barrat, Soft Matter **3**, 685 (2007).
[18] H. K. Moffatt, J. Fluid Mech. **18**, 1 (1964).
[19] J. Koplik and J. R. Banavar, Phys. Fluids **7**, 3118 (1995).
[20] N. V. Priezjev, A. A. Darhuber, and S. M. Troian, Phys. Rev. E **71**, 041608 (2005).
[21] S. Lichter, A. Martini, R. Q. Snurr, and Q. Wang, Phys. Rev. Lett. **98**, 226001 (2007).
[22] B. Ramos-Alvarado, S. Kumar, and G. P. Peterson, Phys. Rev. E **93**, 023101 (2016).
[23] M. Majumder, N. Chopra, R. Andrews, and B. J. Hinds, Nature **438**, 44 (2005).
[24] D. S. Sholl and J. K. Johnson, Science **312**, 1003 (2006).
[25] X. Yong and L. T. Zhang, J. Chem. Phys. **138**, 084503 (2013).
[26] N. Asproulis and D. Drikakis, Phys. Rev. E **84**, 031504 (2011).
[27] S. Lichter, A. Roxin, and S. Mandre, Phys. Rev. Lett. **93**, 086001 (2004).
[28] A. Martini, H.-Y. Hsu, N. A. Patankar, and S. Lichter, Phys. Rev. Lett. **100**, 206001 (2008).
[29] C. Liu and Z. G. Li, J. Chem. Phys. **132**, 024507 (2010).
[30] Z. G. Li, Phys. Rev. E **79**, 026312 (2009).
[31] C. Liu and Z. G. Li, Phys. Rev. E **80**, 036302 (2009).
[32] A. Alizadeh Pahlavan and J. B. Freund, Phys. Rev. E **83**, 021602 (2011).
[33] P. A. Thompson and M. O. Robbins, Phys. Rev. A **41**, 6830 (1990).
[34] J. L. Barrat and L. Bocquet, Faraday Discuss. **112**, 119 (1999).
[35] N. V. Priezjev, Phys. Rev. E **75**, 051605 (2007).
[36] C. Zhang and Y. Chen, Chem. Eng. Process. **85**, 203 (2014).
[37] Y. Chen, C. Zhang, M. Shi, and G. P. Peterson, Appl. Phys. Lett. **100**, 074102 (2012).
[38] C. Zhang, Z. Deng, and Y. Chen, Int. J. Heat. Mass. Transf. **70**, 322 (2014).
[39] C. Zhang, Y. Chen, and G. P. Peterson, Phys. Rev. E **89**, 062407 (2014).
[40] Y. Chen and C. Zhang, Int. J. Heat. Mass. Transf. **78**, 624 (2014).
[41] R. S. Voronov, D. V. Papavassiliou, and L. L. Lee, J. Chem. Phys. **124**, 204701 (2006).
[42] A. Niavarani and N. V. Priezjev, Phys. Rev. E **81**, 011606 (2010).
[43] R. Khare, J. J. D. Pablo, and A. Yethiraj, Macromolecules **29**, 7910 (1996).
[44] S. A. Gupta, H. D. Cochran, and P. T. Cummings, J. Chem. Phys. **107**, 10316 (1997).
[45] N. V. Priezjev, J. Chem. Phys. **127**, 144708 (2007).
[46] S. Plimpton, J. Comput. Phys. **117**, 1 (1995).
[47] J. Sun, W. Wang, and H. S. Wang, J. Chem. Phys. **138**, 234703 (2013).
[48] J. Sun, W. Wang, and H. S. Wang, Phys. Rev. E **87**, 023020 (2013).
[49] R. Khare, J. dePablo, and A. Yethiraj, J. Chem. Phys. **107**, 2589 (1997).
[50] X. Song and J. K. Chen, Int. J. Heat. Mass. Transf. **51**, 1770 (2008).
[51] G. Karniadakis, A. Beskok, and N. Aluru, *Microflows and Nanoflows: Fundamentals and Simulation* (Springer, New York, 2005).
[52] D. C. Rapaport, *The Art of Molecular Dynamics Simulation* (Cambridge University Press, New York, 2004).
[53] N. V. Priezjev, J. Chem. Phys. **136**, 224702 (2012).
[54] J. J. Nicolas, K. E. Gubbins, W. B. Streett, and D. J. Tildesley, Mol. Phys. **37**, 1429 (1979).
[55] J. K. Johnson, J. A. Zollweg, and K. E. Gubbins, Mol. Phys. **78**, 591 (1993).
[56] I. A. Cosden, A Hybrid Atomistic-Continuum Model for Liquid-Vapor Phase Change, Dissertation, University of Pennsylvania, 2013.
[57] M. Thol, G. Rutkai, A. Koster, R. Lustig, R. Span, and J. Vrabec, J. Phys. Chem. Ref. Data **45**, 023101 (2016).
[58] J. P. Hansen and I. R. McDonald, *Theory of Simple Liquids* (Academic Press, New York, 2006).
[59] G. K. Batchelor, *An Introduction to Fluid Dynamics* (Cambridge University Press, New York, 2000).
[60] W. T. Ashurst and W. G. Hoover, Phys. Rev. A **11**, 658 (1975).
[61] N. V. Priezjev and S. M. Troian, J. Fluid Mech. **554**, 25 (2006).